Composites Part B 324 (2026) 113908

Contents lists available at ScienceDirect

Composites Part B

journal homepage: www.elsevier.com/locate/compositesb

Synergistic design of ceramizable and ablation-resistant shape memory oxide-filled phenolic composites for self-adaptive thermal deformation

Likai Hu [a], Fenghua Zhang [a,*], Binghuan Gao [a], Lan Luo [a], Yanju Liu [b], Jinsong Leng [a,**]

[a] Centre for Composite Materials and Structures, Harbin Institute of Technology (HIT), Harbin, 150080, People's Republic of China
[b] Department of Astronautic Science and Mechanics, Harbin Institute of Technology (HIT), No. 92 West Dazhi Street, Harbin, 150000, People's Republic of China

ARTICLE INFO

Keywords:
Ceramization
Composites
Phenolic
Shape memory polymers, Thermal deformation

ABSTRACT

Rapid advancement of deep-space exploration vehicles places increasing demands on smart thermal deformation materials for high efficiency, adaptability, and stability. To solve the shape instability in smart deformable materials at elevated temperatures, a shape memory ceramizable phenolic composite (SMCPC) is proposed by synergistically incorporating the inorganic fillers into a phenolic–boric acid copolymer network. Linear phenolic segments and boric acid serve as the reversible and fixed phases respectively, providing excellent shape memory behavior with a shape recovery rate of 93%. While inorganic functional fillers are employed to trigger high-temperature ceramization, enabling rapid transition from a polymeric system to a mechanically robust ceramic structure. The oxide-filled phenolic composite exhibits a high char yield of 71.7% at 1000 °C, leading to a relative 37.9% increase of the phenolic matrix. At elevated temperatures, the carbonized phenolic matrix promotes thermochemical reduction of oxides, forming a multiphase ceramic framework composed of metal carbides, residual oxides, and graphitized carbon that endows the composite with excellent ablation resistance. Finally, the composite containing 24 wt% HfO_2 exhibits the lowest mass ablation rate of 0.038 g/s, representing a 69.8% reduction compared with the phenolic matrix. Although the material systems show a relative brittleness, the established new strategy of "deformation–recovery–ceramization" enables the potential application of shape memory polymers in extreme environments.

1. Introduction

Shape memory polymers (SMPs) are a representative class of smart materials capable of undergoing programmed shape changes in response to diverse external stimuli such as heat [1–4], light [5–7], magnetism [8,9], and electricity [10,11], endowing them with broad application potential in flexible actuators [12], adaptive structures [13,14], aerospace systems [15], and biomedical fields [16,17]. A conventional thermally induced shape memory cycle typically consists of heating to soften the material, deformation under an applied load, cooling to fix the temporary shape, and subsequent reheating to trigger shape recovery [18–20]. However, materials are required to remain in service for extended periods under coupled high-temperature and mechanical loading conditions even after shape recovery in many engineering applications. In the softened state, the significant reduction in modulus greatly limits their load-bearing capacity and increases the risk of shape instability, which in severe cases may even lead to structural failure.

To address these limitations, various strategies have been explored to improve the high-temperature performance of SMPs, among which the development of heat-resistant SMP systems has attracted particular attention. In recent years, a range of high-temperature SMPs have been reported, such as phthalocyanine resins [21,22], polyimides [23,24], benzoxazines [25], polyether ether ketone [26], and bismaleimides [27]. These materials typically achieve elevated shape-transition temperatures and thermal stability by virtue of highly aromatic backbones or high carbon content. Nevertheless, their long-term resistance to oxidation and ablation in oxygen-rich, high-temperature environments remains insufficient. More importantly, the modulus is difficult to further increase once shape recovery is completed, which limits their ability to sustain structural loads in demanding applications.

In contrast, triggering ceramic transformation in shape memory materials at elevated temperatures has been recognized as a more promising route to simultaneously enhance stiffness and lock the recovered shape [28–30]. Lu et al. [31–34] developed a sintering

* Corresponding author.
** Corresponding author.
E-mail addresses: fhzhang_hit@163.com (F. Zhang), lengjs@hit.edu.cn (J. Leng).

https://doi.org/10.1016/j.compositesb.2026.113908
Received 28 April 2026; Received in revised form 4 June 2026; Accepted 10 June 2026
Available online 15 June 2026

strategy for complex ceramic components based on temperature-responsive polymer composite precursors, providing a pathway toward polymer-derived ceramics. Chen et al. [35] reported shape-memory polymer precursors obtained by copolymerizing epoxy resins with polysiloxanes, which were subsequently converted into ceramics through high-temperature sintering. More recently, Liu et al. [36] introduced polymer-derived ceramic aerogels using polyimide–polysiloxane copolymers as the matrix, enabling an integrated design that couples shape memory behavior with ceramic transformation. Despite these advances, most reported systems rely on siloxane segments to impart ceramicizability. The abundance of low heat-resistant methyl or methoxy groups in such molecular structures restricts the char yield and compromises structural integrity at high temperatures. As a result, their long-term service performance and engineering applicability under extreme thermal conditions remain to be further improved. Furthermore, systematic investigations into the ablation behavior of ceramizable shape memory materials are still lacking, hindering their practical engineering deployment.

Phenolic resin, as a high-performance material for long-term application in aerospace reentry thermal protection systems, offers distinct advantages including abundant raw material sources, high residual carbon content, and outstanding ablation resistance [37–39]. Its significant carbonization at elevated temperatures provides a natural foundation for achieving modulus enhancement and structural stability upon shape memory recovery. Previous work by Leng reported on ablation-resistant shape memory phenolic resins [40], foams [41], and aerogels [42]. However, most related research has focused on shape memory performance or thermal protection capabilities, without addressing how to integrate shape recovery and high-temperature ceramization into a single functional system. Ceramic fillers have attracted considerable attention because of their excellent thermal stability, oxidation resistance, and high melting points. Previous studies have demonstrated that TiO_2 can improve the thermo-oxidative resistance of materials by forming stable oxide layers during ablation [43], while ZrO_2 exhibits outstanding thermal barrier capability and high-temperature structural stability [44–46], which helps maintain the integrity of the ceramic layer. HfO_2 exhibits superior ablation resistance under extreme thermal environments due to its ultrahigh melting point and low oxygen diffusion rate [47,48]. Therefore, developing ceramic-filled shape memory phenolic ceramizable composites (SMCPCs) holds significant importance for expanding the engineering applications of shape memory materials in extreme thermally coupled environments.

Herein, this work reports a SMCPC that integrates ablation resistance, high-temperature tolerance, and excellent shape-memory behavior, aiming to address the critical challenge of achieving stable shapes and structural load-bearing capacity of SMPs after high-temperature recovery. In this system, the shape-memory phenolic–boronic acid copolymer serves dual functions: it acts as the matrix to impart shape memory behavior to the material, while simultaneously functioning as a ceramic precursor that reacts with fillers at elevated temperatures to generate ceramic phases in situ. This design not only enhances the ablation resistance of SMCPCs under extreme high-temperature environments but also endows the material with shape fixation and structural stiffening capability after shape recovery. Notably, a heat conduction model is established to predict the temperature distribution during the ablation process of oxide-filled phenolic composite, providing a theoretical basis for clarifying the ablation enhancement mechanisms induced by different ceramic fillers. As a proof-of-concept study, we preliminarily validate the feasibility of SMCPCs for high-temperature thermoresponsive adaptive shape adjustment.Based on this, an adaptive "deformation–ceramization" strategy is proposed, in which the material can first achieve shape adaptation under thermal stimulation and subsequently transform into a thermally stable ceramic structure in situ. In a word, our work endows shape-memory phenolic-based materials with ceramization capability for the first time. This advancement is expected to promote technological innovation in smart materials for aerospace vehicles while broadening the application scope of SMPs.

2. Experimental

2.1. Raw materials

Formaldehyde solution (37 wt%) was obtained from Aladdin Reagent (Shanghai) Co., Ltd. (China). 4,4-Dihydroxydiphenyl ether, boric acid ($B(OH)_3$), ammonia water, ethanol (EtOH), titanium dioxide (TiO_2) particles, zirconium dioxide (ZrO_2) particles, hafnium dioxide (HfO_2) particles and boron oxide (B_2O_3) particles obtained from McLean Reagent Co., Ltd. (China).

2.2. Synthesis of SMCPCs

The synthesis of shape-memory ceramizable phenolic composites (SMCPCs) was carried out as follows. Initially, 4,4-dihydroxydiphenyl ether was added to a three-necked flask containing ethanol and heated to 60 °C until complete dissolution. Subsequently, a 37 wt% aqueous formaldehyde solution was introduced, and the mixture was stirred until homogeneous. An ammonia solution was then added dropwise to maintain an alkaline environment. The reaction was conducted at 90 °C under a nitrogen atmosphere for 2 h, during which 2 mol of formaldehyde underwent an addition reaction with 1 mol of 4,4- dihydroxydiphenyl ether to form a linear phenolic–formaldehyde oligomer. Afterward, metal oxide (TiO_2, ZrO_2, or HfO_2) particles were blended with boron oxide at a mass ratio of 9:1, and the mixture was incorporated into the reaction system with vigorous stirring to achieve uniform dispersion. Boric acid was subsequently added at a molar ratio of 3:4 relative to linear phenolic-formaldehyde oligomer to realize copolymerization with polymer chains. The reaction was maintained at 100 °C for an additional 2 h, followed by dehydration under reduced pressure to obtain a pre-cured SMCPCs. The resulting prepolymer was poured into molds and cured at 120 °C for 6 h to yield the final SMCPCs. According to the type and loading of metal oxide fillers, a series of composites were prepared, including 12 wt%, 16 wt%, 20 wt%, and 24 wt% TiO_2/SMPF; 12 wt%, 16 wt%, 20 wt%, and 24 wt% ZrO_2/SMPF; and 12 wt%, 16 wt %, 20 wt%, and 24 wt% HfO_2/SMPF, respectively. The detailed formulations of each sample, including the amounts of all raw materials used during the preparation process, are summarized in Table S1.

2.3. Characterization

The chemical structures of SMPF, SMCPCs, and their pyrolyzed products were characterized using a Nicolet iS10 Fourier transform infrared (FTIR) spectrometer (Nicolet Instrument Corp., USA) in transmission mode, with potassium bromide as the background. Spectra were recorded at a resolution of 4 cm^{-1} over the wavenumber range of 4000–500 cm^{-1}. Thermogravimetric analysis (TGA) of SMCPCs was performed using a thermogravimetric analyzer (TGA/DSC1, Mettler-Toledo, Switzerland). Samples with an initial mass of 25–30 mg were heated from 25 to 1000 °C at a rate of 10 °C·min^{-1} under a flowing nitrogen atmosphere. The dynamic mechanical properties of SMCPCs, including the storage modulus and tan δ, were measured using a dynamic mechanical analyzer (DMA Q800, TA Instruments, USA) in tensile mode. Specimens with dimensions of 35 × 2.5 × 1.5 mm^3 were tested in a temperature range of 25–250 °C at a heating rate of 3 °C/min, a frequency of 1 Hz. Tensile properties of SMCPCs were evaluated using a Zwick/Roell Z010 universal testing machine (ZwickRoell GmbH & Co. KG, Germany) with a 5 kN tensile load cell. Dumbbell-shaped specimens were tested at a crosshead speed of 2 mm/min. The flexural properties of SMCPCs were evaluated via three-point bending tests using a Zwick/Roell Z010 universal testing machine (ZwickRoell GmbH & Co. KG, Germany) with a 5 kN tensile load cell. The tests were conducted at a

span-to-thickness ratio of 16:1. The microstructures of SMCPCs were examined using a Tescan scanning electron microscope (Tescan Orsay Holding, Czech Republic) operated in secondary electron mode. Prior to observation, the samples were sputter-coated with a gold layer for 60 s, and the micro-morphologies were observed at magnifications of 200 to 10,000. The microstructure and elemental distribution of the pyrolyzed products were further analyzed using a Thermo Fisher Tecnai G2 F20 transmission electron microscope (Thermo Fisher Scientific Inc., USA); these TEM measurements were conducted by Longjiang Materials Testing Co., Ltd. Oxyacetylene ablation tests of SMCPCs were performed according to the GJB-323A-96 standard. The oxygen and acetylene flow rates were set to 1512 L/h and 1116 L/h, respectively. Cylindrical samples (29.5 ± 0.1 mm in diameter and 10 mm in thickness) were ablated for 50 s. Thermal conductivity and thermal diffusivity were measured using a NETZSCH LFA 467 laser flash analyzer (NETZSCH-Gerätebau GmbH, Germany) using disk specimens of 10 ± 0.1 mm in diameter and 2 mm in thickness. Shape recovery tests of SMCPCs were conducted in a heating oven set to Tg + 20 °C. High-temperature in situ contact angles of SMCPCs were measured using a Dataphysics OCA25-HTV1800 system (Data Physics Instruments GmbH, Germany) over a temperature range of 25–1000 °C at a heating rate of 4 °C/min, without any isothermal holding process. The crystal structures of the pyrolyzed products from SMCPCs were analyzed by X-ray diffraction (XRD) over a 2θ range of 10–90°. XRD patterns were collected using a D8 ADVANCE diffractometer (Bruker, Germany). The elemental composition and chemical states of the products were further investigated by X-ray photoelectron spectroscopy (XPS). XPS analysis was performed using an ESCALAB 250Xi spectrometer (Thermo Fisher Scientific Inc., USA). The thermal conduction simulation of SMCPCs was performed using Python.

3. Results and discussion

3.1. Synthesis and analysis of SMCPCs

The shape memory behavior of SMCPCs is mainly determined by the polymer matrix. The synthesis route of the shape memory phenolic (SMPF) is shown in Fig. 1a. Under alkaline conditions, the linear hydroxybenzene ether reacts with formaldehyde through an addition reaction to form linear phenolic oligomers. After the introduction of boronic acid, the reaction environment changes from alkaline to acidic, promoting the polycondensation reaction between the linear phenolic chains and also enabling copolymerization with boronic acid. In this molecular structure, the linear phenolic segments act as reversible phases, while the boronic acid serves as the fixed phase. This molecular design endows phenolic resins with shape memory properties.

Fig. 1b illustrates the manufacturing process of SMCPC, where inorganic metal oxide powders are introduced during the polymer synthesis process. The hydroxyl groups on the surface of the inorganic particles enable them to interact with the polymer chains through hydrogen bonds during the mixing process, thereby ensuring an effective bond. Fig. S1 shows the FTIR spectra of SMPF and various SMCPCs. The absorption band at 790 cm^{-1} corresponds to the ortho-substituted C–H vibration of the benzene ring, while the peak at 1020 cm^{-1} is attributed to the stretching vibration of ph–CH_2–OH groups. In addition, the characteristic ph–O–ph stretching vibration at 1220 cm^{-1} confirms the formation of ether linkages, which indicates successful addition reactions between formaldehyde and 4,4′-diphenyl ether, and a distinct B–O stretching vibration at 1370 cm^{-1} evidences copolymerization between the phenolic monomers and boric acid. These spectral features collectively confirm the synthesis of SMPF. Notably, the FTIR spectra of SMCPCs closely match those of pristine SMPF, indicating that the incorporation of inorganic functional particles does not alter the chemical structure of the polymer matrix. The microstructures of the SMCPCs are shown in Fig. S2. In all three systems, the inorganic particles

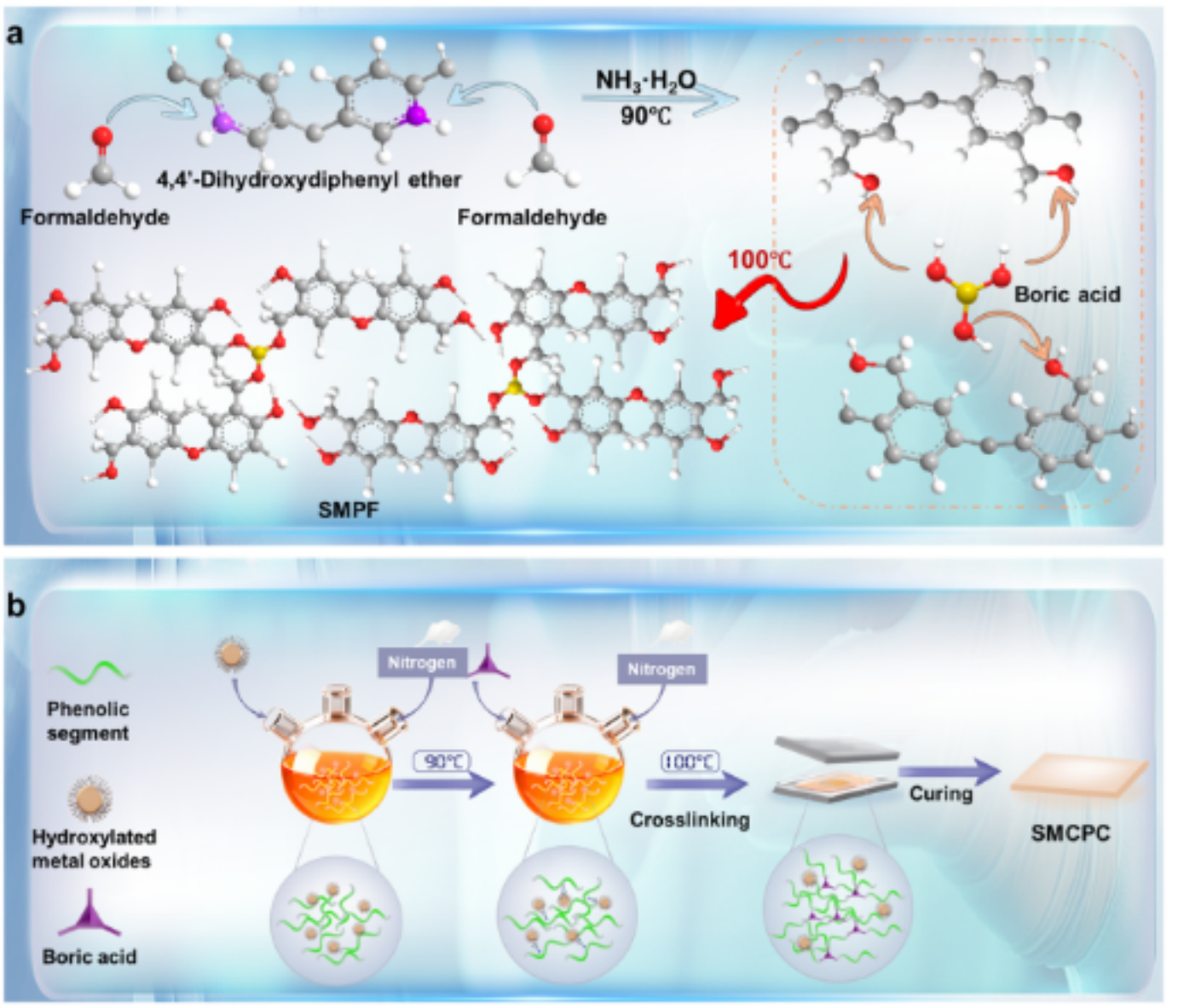

Fig. 1. The multiscale design of SMCPC a) Schematic illustration for the synthesis of SMPF. b) Schematic illustration for the preparation of SMCPC.

are uniformly embedded in the SMPF matrix. No phase separation or bubble formation was observed in the SEM images, which indicates the inorganic particles are well dispersed in the matrix.

3.2. Thermomechanical properties and shape memory characteristics of SMCPCs

The shape memory behavior of SMCPCs originates from temperature-induced changes in polymer chain mobility. We undertook a systematic DMA investigation prior to evaluating shape memory performance to probe the influence of inorganic fillers on the segmental dynamic mechanical properties of the SMPF matrix. Figure S3 and Fig. 2 (a–f) illustrate the characteristics of the storage modulus and the tan δ of SMPF and SMCPCs as they vary with temperature. The tan δ curve of SMPF shows a clear single peak, and its *Tg* is located at 89 °C, which corresponds to the transition between glassy state to rubbery state of the phenolic matrix. After adding ceramic particles, all the SMCPCs still show one tan δ peak which indicates that the addition of the inorganic filler is unable to change the intrinsic phase transition behaviour of the system and hence its shape memory response is still dominated by the phenolic matrix.

The tan δ peak position of SMCPC shifts progressively toward higher temperatures relative to that of pristine SMPF. As the ceramic content increases from 12 wt% to 24 wt%, *Tg* rises to the range of 94–144 °C. This indicates that the presence of the ceramic filler has led to an increase in the energy required for the chain segment movement. At the same time, the peak becomes wider as the ceramic content increases, suggesting that the ceramic particles restrict the coordinated movement of the molecular chain segments. This phenomenon can be consistently observed in all three SMCPC systems, indicating that the incorporation of different ceramic fillers leads to a slight reduction in the shape memory performance.

At room temperature, SMPF exhibits a storage modulus of approximately 2.1 GPa, which decreases sharply upon heating through the glass transition region, consistent with the typical thermomechanical behavior of SMPs. SMCPCs exhibit a higher storage modulus at room temperature. With a ceramic content of 12 wt%, the room-temperature storage modulus increases to approximately 3 GPa, and further enhancement is observed as the filler content rises to 24 wt%. The storage modulus of SMCPC at room temperature increased by approximately 20% to 40% with the increase of ceramic content. These results indicate that the incorporation of ceramic particles effectively enhances the stiffness of the composite material while retaining the phase transformation characteristics of the SMPF matrix. The increase in Tg and the broadening of the tan δ peak provide a higher activation threshold and a wider operating temperature range for shape recovery, which is beneficial for SMCPCs that require thermally stable shape memory performance.

As shown in Fig. 2g, 20 wt% TiO_2/SMPF can complete the shape recovery process at 120 °C within approximately 40 s. Similarly, the 20 wt% ZrO_2/SMPF sample also achieves shape recovery in about 40 s (Fig. S4, Videos S1–2). These results indicate that, after the incorporation of an appropriate amount of ceramic fillers, the SMCPCs are still capable of realizing shape recovery. To further investigate the effect of ceramic filler loading on the shape memory performance of SMCPCs, the shape fixity and shape recovery ratios at different filler contents were systematically analyzed (Fig. 2h–i). The results indicate that all samples exhibit excellent shape fixity (97.2%–99.1%), which shows a slight

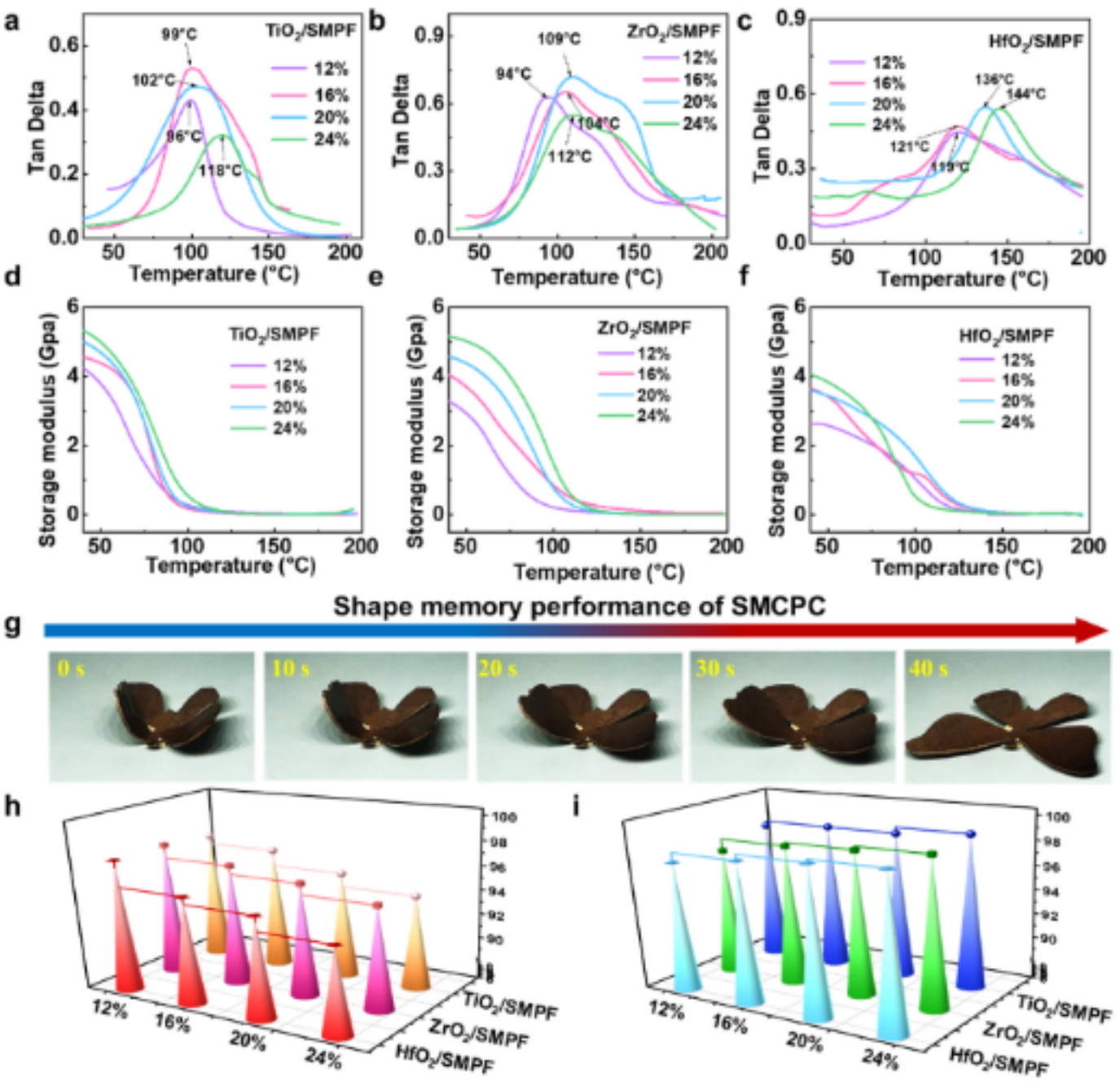

Fig. 2. Dynamic Mechanical Properties and Shape Memory Properties of SMCPCs. The tan δ curves of a) TiO_2/SMPFs, b) ZrO_2/SMPFs, and c) HfO_2/SMPFs. The storage modulus curves of d) TiO_2/SMPFs, e) ZrO_2/SMPFs, and f) HfO_2/SMPFs. g) The shape recovery process of 20 wt% TiO_2/SMPF. h) The shape recovery rate of SMCPCs. i) The shape fixation rate of SMCPCs.

increasing trend with increasing ceramic filler content. This trend can be attributed to the incomplete relaxation of polymer chain segments induced by the incorporation of ceramic fillers, which directly leads to the gradual decrease in the shape recovery ratio with increasing filler content.

The effect of ceramic filler content on the shape recovery speed was further investigated using TiO_2/SMPFs as a representative system, and the corresponding results are shown in Fig. S5. The results demonstrate that the four TiO_2/SMPFs with increasing ceramic contents (12 wt%、16 wt%、20 wt%、24 wt%) exhibited maximum deformation strains of 12.46%, 10.19%, 8.89%, and 7.91% under the same 1.5 N loading condition, respectively, indicating progressively reduced deformability with increasing ceramic filler content. Moreover, the recovery speed decreases noticeably with increasing ceramic content. Among them, the 12 wt% TiO_2/SMPF sample shows the fastest recovery behavior and reaches approximately 90% shape recovery within 200 s, followed by a gradual slowdown in the later stage. In contrast, the 24 wt% TiO_2/SMPF sample requires more than 250 s to reach 90% recovery. These results directly confirm that the restriction of molecular segment mobility induced by ceramic fillers slows the recovery speed of SMCPCs.

Based on the above discussion of the shape memory performance of SMCPCs, the incorporation of ceramic fillers influences the shape memory performance of SMCPCs in four aspects: (i) increasing Tg, (ii) broadening the tan δ peak, (iii) reducing shape recovery speed, and (iv) decreasing the final shape recovery ratio, while still maintaining shape memory performance.

3.3. The mechanical properties and thermal stability of SMCPCs

As a ceramizable composite material, SMCPC is usually used in practical applications under stress conditions or in complex working environments. Therefore, the tensile and bending properties of SMCPCs with different ceramic particles and filling contents were discussed. The tensile stress–strain curves of SMCPCs with varying ceramic particle systems and filler ratios is shown in Fig. 3(a–c). All composite materials exhibit a distinct linear elastic region followed by a sudden fracture, which reflects the brittle fracture characteristic of phenolic-based composite materials. As the content of ceramic particles increased from 12 wt% to 20 wt%, in all three SMCPC systems, the tensile strength and tensile modulus continued to rise steadily. At a filler content of 20 wt%, the fracture strengths of each system reached their maximum values of 121.46 MPa, 151.99 MPa and 124.69 MPa respectively. Further increasing the content of ceramic particles to 24 wt%, although the elastic modulus of the three systems remained relatively high, the tensile strengths all decreased to varying degrees. The microstructure of SMCPCs with 24 wt% ceramic filler (Fig. S6) explains this phenomenon. Excessive ceramic particles aggregated within the matrix, disrupting the continuity of the structure. Under tensile loading, these aggregated areas became stress concentration points that promotes crack formation and accelerates the fracture process.

The bending strength of SMCPCs with different ceramic particle systems and filler contents is illustrated in Fig. 3(d–f). All composite materials exhibit higher load-bearing capacity under bending loads. Similar to the results of tensile tests, the bending strength increases significantly as the ceramic filler content increases from 12 wt% to 20 wt %. However, a further increase in filler content to 24 wt% leads to a decline in bending strength. To further evaluate the influence of ceramic fillers on the brittleness of SMCPCs, the bending strain-to-failure results are presented in Fig. 3(d–f). For all three SMCPC systems, the strain-to-failure gradually decreases with increasing ceramic filler content, and the downward trend becomes increasingly evident at higher filler loadings. In the TiO_2/SMPF system, the strain-to-failure decreases from 2.97% at 12 wt% filler loading to 1.16% at 24 wt% filler loading. These results indicate that increasing filler content enhances the brittleness of the composites and reduces their deformation capacity. Considering both the bending strength and strain-to-failure results, the 20 wt% filler loading exhibits relatively better mechanical performance among the four formulations investigated in this study, providing a reasonable balance between load-bearing capability and brittleness. This mechanical robustness provides a solid foundation for applications of SMCPC in high-temperature load-bearing components and shape memory structures.

For SMCPCs, their thermal degradation behavior determines the upper limit of their usage temperature and directly affects the stability of

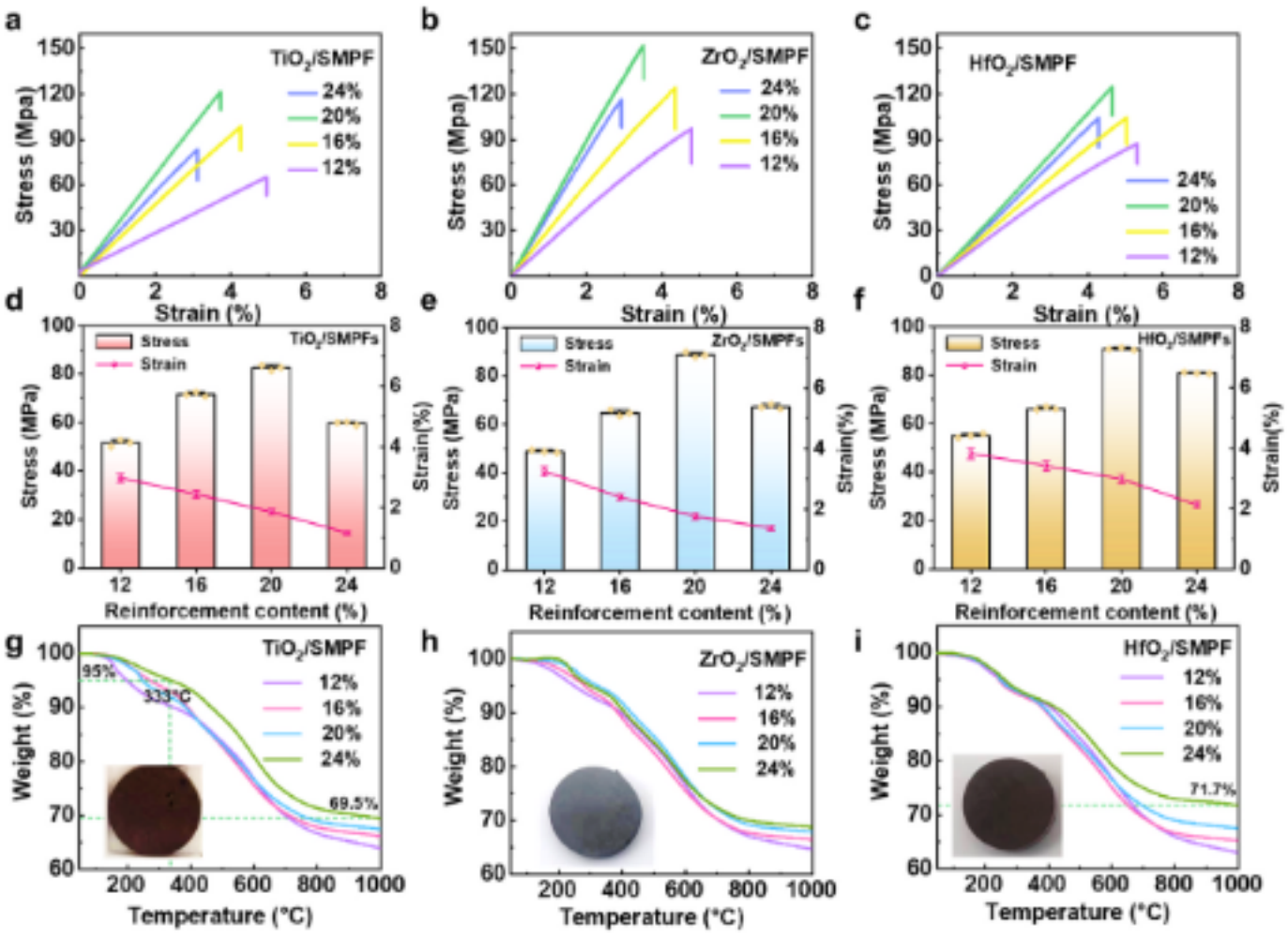

Fig. 3. Mechanical properties and thermal stability of SMCPCs. a) The tensile stress-strain curves of TiO_2/SMPFs. b) The tensile stress-strain curves of ZrO_2/SMPFs. c) The tensile stress-strain curves of HfO_2/SMPFs. d) Bending strength and strain-to-failure of TiO_2/SMPFs. e) Bending strength and strain-to-failure of ZrO_2/SMPFs. f) Bending strength and strain-to-failure of HfO_2/SMPFs. g) The TGA curves of TiO_2/SMPFs. h) The TGA curves of ZrO_2/SMPFs. i) The TGA curves of HfO_2/SMPFs.

the material during the high-temperature transformation process. TGA tests were performed on SMPF and SMCPCs with different filler loadings (12 wt%, 16 wt%, 20 wt%, and 24 wt%) of TiO_2/SMPF, ZrO_2/SMPF, and HfO_2/SMPF under a constant nitrogen flow atmosphere, to investigate the effect of ceramic particle incorporation on their thermal stability. The results are shown in Figures S7 and 3(g-h). The overall thermal degradation behavior of SMCPCs is similar to SMPF, which indicates that the thermal degradation is mainly related to the SMPF matrix. Below 300 °C, only a small amount of mass loss is observed, which can be attributed to the removal of low-molecular-weight volatile substances. Between 300 °C and 800 °C, rapid mass loss occurs due to the breakage of the phenolic framework and the release of gas products. When heated further to above 800 °C, the mass loss rate significantly decreases, and the system gradually enters a stable carbonization stage.

Notably, the temperature corresponding to 5% weight loss for SMCPCs reaches approximately 333 °C, and the SMPF matrix retains a char yield of about 52% at 1000 °C, which indicates that SMPF is suitable for high-temperature environments and has excellent carbonization capabilities. SMCPCs maintain a higher residual quality throughout the heating process. At 1000 °C, the char yield increases with the increase in ceramic particle content, reaching a maximum of 71.7%, and maintains a stable macroscopic structure, as shown in the inset images of Fig. 3(g and h). This enhancement is due to the thermal stability of the ceramic particles under inert conditions and their reinforcing effect on the carbonization framework, thereby maintaining the continuity of the structure at high temperatures.

The DTG curves provide further insight into the decomposition processes of SMPF and SMCPCs. As illustrated in Figs. S8–S9, SMPF exhibits three distinct peaks, which corresponds to the sequential breakdown of the phenolic network. After ceramic particle incorporation, these peaks shift slightly toward higher temperatures and become progressively broader with increasing filler content, which demonstrates a delayed and more gradual decomposition process. This characteristic indicates that SMCPCs have a stronger resistance to rapid thermal degradation, which is beneficial for maintaining structural integrity under conditions of rapid heating or thermal shock.

3.4. Ceramic Filler–Regulated ablation resistance mechanisms of SMCPCs

Phenolic resin is widely employed as the matrix material for the atmospheric re-entry thermal protection system of spacecraft return capsules due to its excellent ablative performance. However, the introduction of the flexible segments to achieve the shape memory function inevitably weakened the ablation resistance of the phenolic resin. This work alleviated the negative effects caused by the flexible chain segments by introducing inorganic ceramic fillers.

Under heat flux, pyrolysis, char formation, and ablation sequentially occur within SMCPCs [49]. The imposed high heat flux firstly interacts with the material surface and leads to the formation of an ablative layer. Subsequently, the heat conducts inward through the dense char layer, where it accumulates and penetrates into the pyrolysis zone and the virgin region. As energy accumulates within the material, the pyrolysis zone continuously expands, driving the ablation front inward and resulting in an increase in ablation depth. Since heat transfer plays a dominant role in the ablation process, a simplified model based on the heat conduction equation combined with the Arrhenius equation was established to elucidate the internal thermal distribution during pyrolysis and ablation, and to further assess the effects of three different ceramic fillers on the ablation resistance of phenolic composites. In addition, other heat-transfer mechanisms such as the thermal radiation, gas convection, pyrolysis gas blowing, surface recession, which primarily affect heat transfer on the surface rather than its interior and were therefore equivalently represented using the effective thermal diffusivity and empirical thermal-resistance attenuation equation.

The model describes a cylindrical specimen with height H and radius R under the conditions that the specimen was kept at an environment with uniform temperature T_0 and a constant heat source T_1 applied on the top surface. Previous studies have demonstrated that heat conduction is the dominant mode of heat transfer, therefore, thermal radiation and other heat transfer mechanisms are neglected in this model [50]. Under this assumption, the temperature T is expressed as a function of time t and spatial coordinate z:

$$\frac{\partial T}{\partial t} = \gamma \frac{\partial^2 T}{\partial z^2}, 0 < z < H \tag{1}$$

The initial condition is defined as: at

$$t = 0, T = T_0. \tag{2}$$

Where z denotes the spatial coordinate, γ is the thermal diffusivity (m^2/s), and T_0 is the initial temperature (K). Assuming adiabatic conditions at the lateral surface and bottom, the boundary conditions are given by:

At the bottom surface ($z = 0$), the boundary condition is:

$$\frac{\partial T}{\partial z}\Big|_{z=0} = 0 \tag{3}$$

At the top boundary ($z = H$), heat flux follows a Gaussian distribution, where the maximum temperature occurs at the center (T_1) and gradually decreases along the radial direction, the boundary condition is:

$$T(H, t) = T_1 \tag{4}$$

The analytical solution to equations (1)–(4) is expressed as:

$$T(z,t) = T_0 + (T_1 - T_0)\left[1 - \sum_{i=0}^{\infty} \frac{4}{(2n+1)\pi}(-1)^n \exp\left(-\gamma \frac{(2n+1)^2\pi^2}{4H^2} t\right)\cos\left(\frac{(2n+1)\pi z}{2H}\right)\right] \tag{5}$$

Where $n = 0,1,2,3,\ldots$, H is the thickness of the cylindrical specimen (m), and T_1 is the constant temperature of the top heat source (K). The measured thermal diffusivities of the three composite materials are listed in Table S2. Under the same filler loading, HfO_2/SMPF exhibits the lowest thermal diffusivity of 0.184 ± 0.03 mm^2/s, whereas TiO_2/SMPF shows a comparatively higher thermal diffusivity. Based on the analytical solution of the above heat conduction equation, the Explicit Finite Difference Method was employed to visualize the temperature field distribution. The internal temperature point cloud of the three composites ablated for 50 s are shown in Fig. 4(a–c). Due to the influence of the three ceramic fillers on heat transfer resistance, the thermal diffusivities of TiO_2/SMPF, ZrO_2/SMPF, and HfO_2/SMPF are 0.224 mm^2/s, 0.198 mm^2/s, and 0.184 mm^2/s, respectively, showing a decreasing trend. Accordingly, the high-temperature region at the top of the three materials gradually becomes more confined.

Meanwhile, the temperature profile results of the internal cross-sections indicate that after ablation for 50 s (Fig. 4d–f), the internal temperature field exhibits a pronounced non-uniform distribution along the Z direction. As the depth increases, the temperature gradually decreases, which leads to a significant temperature gradient attenuation. In addition, the spatial extent of the high-temperature region shrinks with increasing depth, indicating a progressively narrowing heat-affected zone. Notably, the HfO_2/SMPF exhibits the narrowest high-temperature region width and the smallest affected thickness, demonstrating the best thermal insulation performance among the three materials.

Under high-temperature conditions, the nonlinear thermal decomposition evolution of phenolic resin from the polymer state to complete carbonization can be described by the Arrhenius equation, where the pyrolysis rate k is given as:

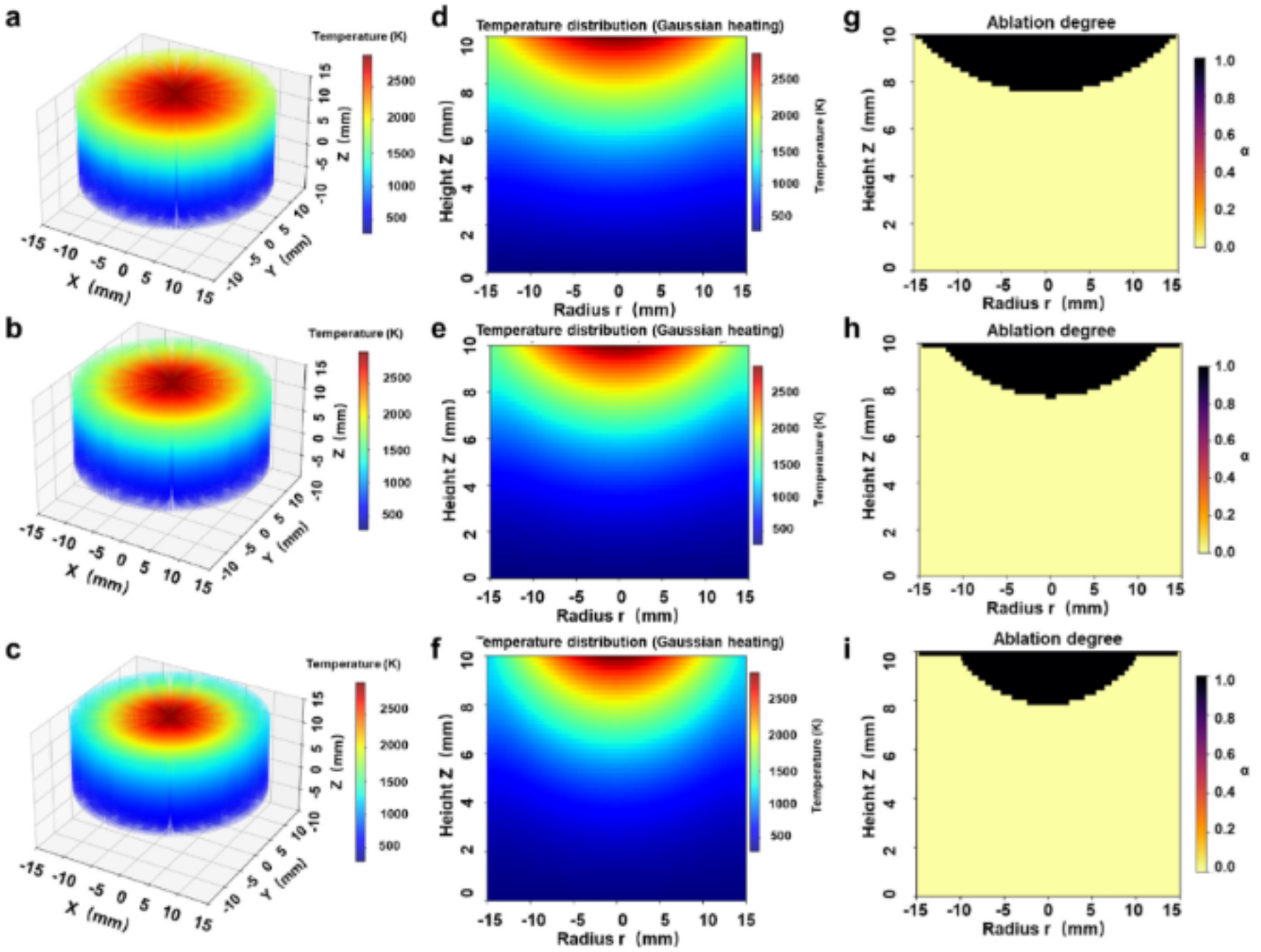

Fig. 4. Simulation of temperature distribution and composite ablation based on the thermal conductive equation in a cylinder model. The internal temperature contour plots of a) 20 wt% TiO_2/SMPF, b) 20 wt% ZrO_2/SMPF and c) 20 wt% HfO_2/SMPF after 50 s of ablation. Cross-sectional internal temperature distribution of d) 20 wt% TiO_2/SMPF, e) 20 wt% ZrO_2/SMPF, and f) 20 wt% HfO_2/SMPF after 50 s of ablation. Visualized distribution of the conversion degree for g) 20 wt% TiO_2/SMPF, h) 20 wt% ZrO_2/SMPF, and i) 20 wt% HfO_2/SMPF after 50 s of ablation.

$$k = A\exp\left(-\frac{E_a}{RT}\right) \tag{6}$$

Combined with the first-order reaction rate equation:

$$\frac{d\alpha}{dt} = k(1-\alpha) \tag{7}$$

where A is the pre-exponential (frequency) factor, E_a is the activation energy for the thermal decomposition of the SMCPC (J/mol), R is the universal gas constant (J/mol·K), and T is the material temperature (K), α is the conversion degree of phenolic resin. The activation energy of SMCPCs is summarized in Table S3. At an identical filler loading, HfO_2/SMPF exhibits the highest thermal decomposition activation energy of 80880.0 J/mol, indicating that more energy is required to initiate thermal decomposition, whereas TiO_2/SMPF shows a relatively lower activation energy.

A visualized distribution of the conversion degree α can be obtained through time-integration discretization process. In addition, within this model, the ablation depth $h_{ablation}$ is defined as the maximum depth measured from the top surface of the cylinder where $\alpha \geq 0.9$, corresponding to the region in which the material has undergone near-complete ablation. For each radial position, α is evaluated layer by layer along the Z direction starting from the top surface. The location where α first drops below 0.9 is identified, and the vertical distance from this position to the top surface is defined as $h_{ablation}$, as illustrated in Fig. 4(g–i). Among the three material systems, HfO_2/SMPF exhibits the smallest ablation depth, while TiO_2/SMPF shows the largest, which is consistent with the trends observed in the temperature distribution results.

Cylindrical SMCPC specimens containing 20 wt% ceramic particles were selected and subjected to a 50 s oxyacetylene ablation test to evaluate their protective capability and structural stability under extreme heat flux conditions (Video S3), while further confirming the regulatory effect of different ceramic fillers on the ablation resistance of the materials. During the initial stage of the ablation process, the intense heat flux causes the surface temperature to rise rapidly and triggers the thermal degradation of the SMPF matrix. The strong heat absorption effect and the release of gas products delay the transfer of heat to the composite material layer. As the ablation progresses, a continuous ceramic layer gradually forms on the surface of the matrix, which to some extent prevents the further transfer of heat and helps maintain the structural integrity of the SMCPCs. The changes in surface temperature during the ablation process are shown in Fig. 5(a–c), all samples exhibited rapid temperature increase in the early stage. The surface temperature of TiO_2/SMPF reached a maximum of 2100 °C, while that of HfO_2/SMPF reached a higher peak of 2600 °C. Lower surface temperatures do not necessarily indicate better ablation resistance. For TiO_2/SMPF, the lower surface temperature is associated with its more intense ablation behavior (the highest ablation rate compared with other two materials) and phase transformation of TiO_2. Intense matrix pyrolysis, repeated destruction of the carbon layer, melting of the ceramic layer and continuous material removal consume a large amount of heat energy, limiting the increase in surface temperature. In contrast, ZrO_2/SMPF and HfO_2/SMPF can form stable ceramic-carbon composite layers at high temperatures, which can effectively inhibit further ablation and allow the incident heat to accumulate on the surface.

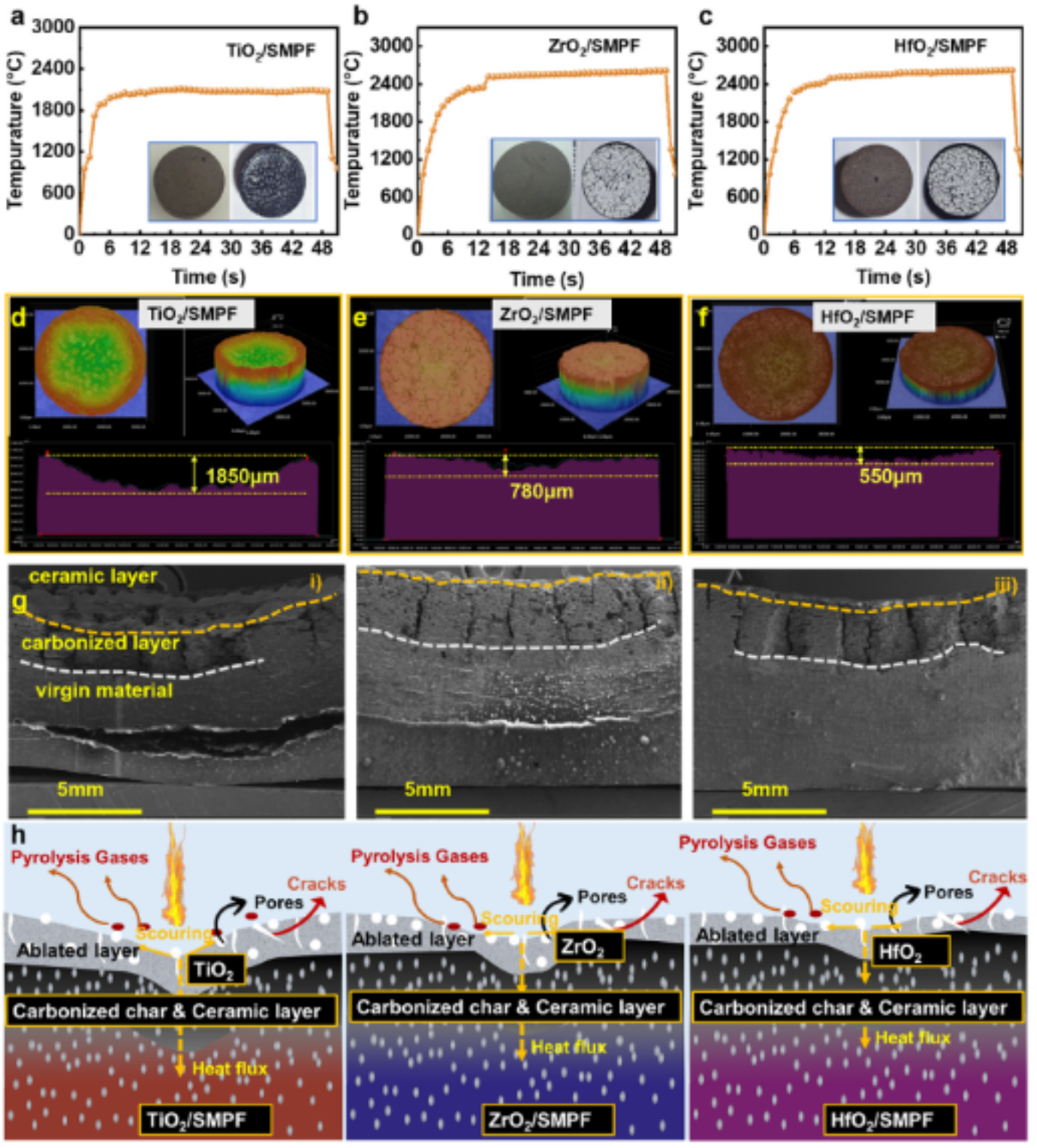

Fig. 5. Ablative properties of SMCPCs. a) The ablative test curves of 20 wt% TiO_2/SMPF. b) The ablative test curves of 20 wt% ZrO_2/SMPF. c) The ablative test curves of 20 wt% HfO_2/SMPF. d-f) The three-dimensional depth of field pictures of SMCPCs. g) The cross-sectional SEM morphologies of i) 20 wt% TiO_2/SMPF, ii) 20 wt% ZrO_2/SMPF, and iii) 20 wt% HfO_2/SMPF. h) The ablative mechanism of SMCPCs.

The images before and after the test (the inset parts of Fig. 5a–c) as well as the three-dimensional depth-field micrographs (Fig. 5d–f) show that all the samples have obvious central erosion pits, with significant differences in depth. The erosion of TiO_2/SMPF is the most severe, with an ablation depth of approximately 1850 μm, while HfO_2/SMPF presents a relatively shallow pit-like structure with a depth of approximately 550 μm. This indicates that the introduction of HfO_2 is more effective in significantly inhibiting the ablation and peeling processes of the material. The ablation performance parameters obtained from the tests were in agreement with the aforementioned observations (Table S4) and the ablation behavior predicted by the thermal diffusion model. After 50 s of ablation, the linear ablation rate and mass ablation rate of HfO_2/SMPF were the lowest, at 0.011 mm/s and 0.045 g/s respectively, demonstrating the most outstanding ablation resistance. The performance of ZrO_2/SMPF was at an intermediate level, with ablation rates of 0.028 mm/s and 0.058 g/s respectively, while the protective performance of TiO_2/SMPF was weaker, with corresponding ablation rates of 0.037 mm/s and 0.078 g/s.

To further clarify the ablation-resistance mechanism of different ceramic systems, the cross-sectional SEM morphologies of the ablated samples were analyzed, as shown in Fig. 5g and S10. All SMCPCs formed a multilayer structure after ablation, consisting of an outer ceramic layer, an intermediate carbonized layer, and the underlying virgin material. The TiO_2/SMPF sample exhibited a relatively thin and loose ceramic layer with a large number of cracks and obvious interfacial discontinuities. In particular, large cracks were observed in the resin layer due to non-uniform thermal shrinkage during ablation. In contrast, such large cracks were not observed in the cross-sections of the ZrO_2/SMPF and HfO_2/SMPF samples.

Moreover, the interfaces between adjacent layers in the ZrO_2/SMPF and HfO_2/SMPF samples were less distinguishable, and the interface between the ceramic layer and carbonized layer was more continuous. Comparison of the surface SEM morphologies between the TiO_2/SMPF and HfO_2/SMPF ablated samples further revealed that both systems exhibited relatively uniform elemental distributions after ablation (Fig. S11). The TiO_2/SMPF sample showed a relatively smooth surface, which can be attributed to a melting–solidification process during ablation. In contrast, the HfO_2/SMPF sample exhibited lower crack density and narrower crack width, indicating the formation of a more compact and denser ceramic layer. The dense ceramic barrier effectively suppressed crack propagation and reduced oxygen and heat penetration into the matrix, thereby enhancing the thermal insulation capability and structural stability during ablation. These observations provide direct microstructural evidence for the better ablation resistance of the HfO_2/SMPF. Based on these observation results, the ablation behaviors of the three SMCPCs are schematically illustrated in Fig. 5h.

All SMCPCs outperformed the previously reported shape-memory phenolic resins as well as other shape-memory polymer materials and

composite systems. The improved ablation resistance can also be attributed to the formation of a relatively dense multiphase ceramic barrier during high-temperature exposure, which effectively suppresses oxygen penetration and alleviates thermochemical erosion of the internal matrix [51]. The performance differences among these three SMCPCs arise from their different high-temperature phase stability and the integrity of the protective layer formed during ablation. The surface of HfO_2/SMPF forms a dense HfO_2 layer with extremely high melting point and excellent thermal stability, which can effectively resist heat flow and oxidation erosion [48]. Previous studies have shown that ZrO_2 can promote the densification of the carbonization layer and maintain the integrity of the ablation layer through its stable high-temperature oxidation phase [44]. However, TiO_2 undergoes phase transformation under extreme heat conditions and forms a polycrystalline oxide prone to microcracks, which will disrupt the continuity of the protective layer and is difficult to prevent heat penetration [43]. Therefore, HfO_2/SMPF has the best ablation resistance, while TiO_2/SMPF provides relatively weaker protection. Regardless of this, the incorporation of ceramic particles always enhances the ablation resistance of shape memory phenolic composite materials.

Lightweightness is a critical requirement for aerospace thermal protection materials, the influence of ceramic filler loading on the density of SMCPCs was investigated. Fig. S12 shows the density variation of SMCPCs with different filler contents. The density of pristine SMPF was 1.36 g/cm^3. With increasing ceramic filler loading, the density of SMCPCs gradually increased due to the intrinsically higher density of the ceramic particles. Among all formulations, the highest density was observed for 24 wt% HfO_2/SMPF, reaching 1.63 g/cm^3, while the densities of 24 wt% TiO_2/SMPF and 24 wt% ZrO_2/SMPF were 1.59 g/cm^3 and 1.60 g/cm^3, respectively. Despite the increase in density caused by filler incorporation, the overall density variation remained relatively limited, suggesting that the lightweight characteristics of the composites were retained. The influence of ceramic filler loading on the ablation resistance of the HfO_2/SMPF system was further investigated, and the results are summarized in Table S5. As the ceramic filler content increased, both the mass ablation rate and linear ablation rate decreased progressively, indicating a continuous improvement in ablation resistance. The pristine SMPF exhibited a mass ablation rate of 0.126 g/s. Upon incorporation of 12 wt% HfO_2, the mass ablation rate decreased to 0.080 g/s. With a further increase in filler loading to 24 wt%, the mass ablation rate was reduced to 0.038 g/s corresponding to a reduction of approximately 69.8% compared with pristine SMPF. In contrast, the density increased from 1.36 g/cm^3 for SMPF to 1.63 g/cm^3 for 24 wt% HfO_2/SMPF, representing an increase of approximately 19.8%. These results suggest that the improvement in ablation resistance provided by ceramic fillers is considerably more significant than the associated increase in density, making ceramic filler incorporation an effective strategy for optimizing the performance of SMCPCs in high-temperature aerospace deformation structures.

3.5. Ceramization pathways and material evolution of SMCPCs

The high-temperature stability of SMCPC provides the structural basis for its ceramization. By subjecting SMCPCs to thermal treatment in a tube furnace under a nitrogen atmosphere, the polymer pyrolysis, carbonization, and inorganic phase reactions can be carried out under controllable conditions (Fig. 6a). Due to its excellent processability and shape memory properties, SMCPCs can be formed into complex temporary shapes. When heated in the tube furnace, the samples successively undergo shape memory recovery and ceramization transitions,

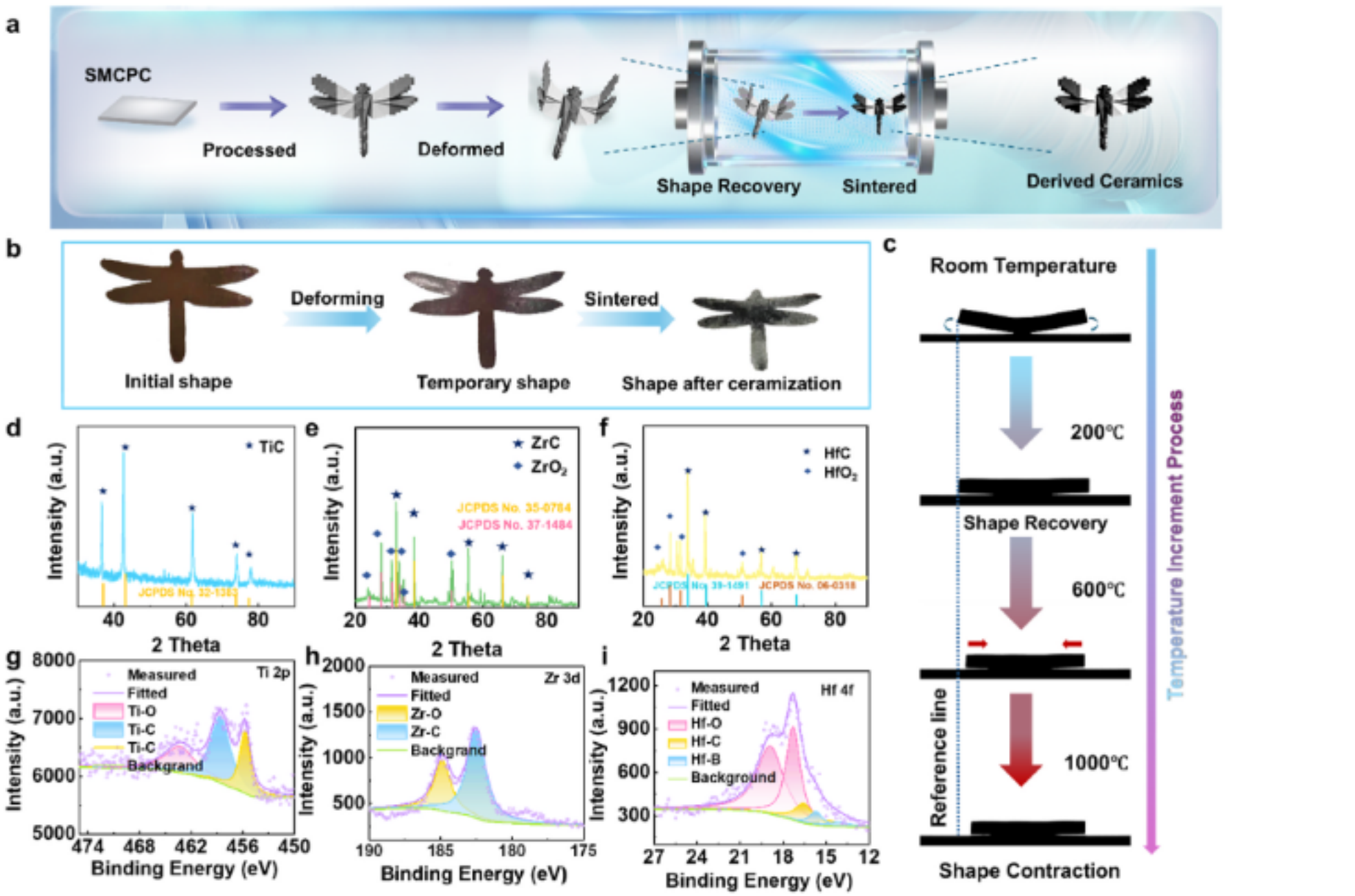

Fig. 6. Analysis of the heat treatment process for SMCPCs. a) The schematic of sintering SMCPCs with temporary shapes in a tube furnace. b) The images of SMCPCs before and after sintering. c)The visualization of high-temperature contact angle images during sintering of SMCPCs. d-f) The XRD analysis of SMCPCs sinter products. g-i) The XPS analysis of SMCPCs sinter products. (All tested samples contained 20 wt% ceramic fillers.)

ultimately generating SMCPC-derived ceramics, as shown in Fig. 6b. Through in-situ high-temperature observation of the V-shaped specimens (Fig. 6c), the ceramization process of SMCPCs was recorded more clearly. It began to recover its shape at a relatively low temperature (120 °C), and recovered to its original shape within 40 s. As the temperature was further increased, the sample showed a gradual reduction in size while maintaining its macroscopic shape. At higher temperatures, the sintering process was completed, resulting in a ceramic body with mechanical stability.

The sintered samples were analyzed by XRD to identify the phase composition after ceramization, with the results illustrated in Fig. 6d–f. All ceramicized specimens exhibit sharp and intense diffraction peaks, indicating that the composites adopt a predominantly crystalline structure after high-temperature treatment, with well-defined crystalline phases. Comparison with standard PDF cards shows that the characteristic diffraction peaks of the ceramicized TiO_2/SMPF, ZrO_2/SMPF, and HfO_2/SMPF can be respectively indexed to their corresponding carbides TiC (PDF# 32-1383), ZrC (PDF# 35-0784), and HfC (PDF# 39-1491). Additionally, the diffraction features associated with residual ZrO_2 and HfO_2 are also observed in the ceramicized ZrO_2/SMPF and HfO_2/SMPF samples. XPS analysis was conducted on the ceramicized samples to investigate the chemical bonding state of the products (Fig. 6g–i). The Ti 2p, Zr 3d, and Hf 4f spectra all showed the coexistence of metal-carbon bonds and metal-oxygen bonds, confirming the simultaneous presence of carbides and oxides. These test results confirmed that SMCPC underwent multiphase evolution during the ceramization process, including polymer carbonization, carbon thermal reduction of metal oxides, and incomplete conversion of oxides to carbides.

During the high-temperature heat treatment process, SMCPC gradually transforms from an organic polymer to an inorganic ceramic structure. This process involves complex chemical reactions and phase transitions. The possibility of potential reactions was evaluated using the HSC chemical software, and the related reaction sets are listed in Table S6. In the TiO_2/SMPF system, increasing the temperature promotes the continuous carbonization process of the resin, while the B_2O_3 can act as a liquid-phase flux at elevated temperatures, thereby promoting interfacial diffusion and facilitating ceramic densification [52, 53]. In addition, a small amount of B_2O_3 slightly regulates the reaction pathway. Thermodynamic calculations (Fig. 7a) indicate that most reactions become favorable above 1500 °C ($\Delta G < 0$), among which the reaction where TiO_2 directly undergoes carbon thermal reduction to form TiC has the strongest driving force, and this force increases with the increase in temperature. This result is consistent with the main TiC diffraction observed in XRD and the Ti–C bond present in XPS, confirming that TiC is the main ceramic phase. Microstructural observation further proves this mechanism. As shown in Fig. 7d, TEM and element distribution maps show uniform distribution of Ti, C, and O, with relatively low boron content. High-resolution TEM shows that the ceramic particles are encapsulated by multiple layers of graphitized carbon, and the selected area electron diffraction (SAED) pattern shows typical polycrystalline rings, indicating that this is a multiphase ceramic network composed of TiC, residual TiO_2, and graphitized carbon.

The ZrO_2/SMPF system exhibits a similar and component-dependent evolution process (Fig. 7b). Thermodynamic analysis indicates that within the lower temperature range, the ΔG values of reactions #6 and #7 are relatively low, so they are prioritized, resulting in the early consumption of B_2O_3. The boron content is limited, and their influence on the final phase composition is minor. At higher temperatures, carbon thermal reduction becomes the main reaction pathway for ZrO_2, generating ZrC. Therefore, the ceramicized product is mainly composed of ZrC and the remaining ZrO_2. The corresponding TEM results (Fig. 7e) show the uniform distribution of C, Zr, O, and B elements. Clear lattice stripes are observed in the high-resolution images, while the SAED spectra show typical polycrystalline diffraction rings.

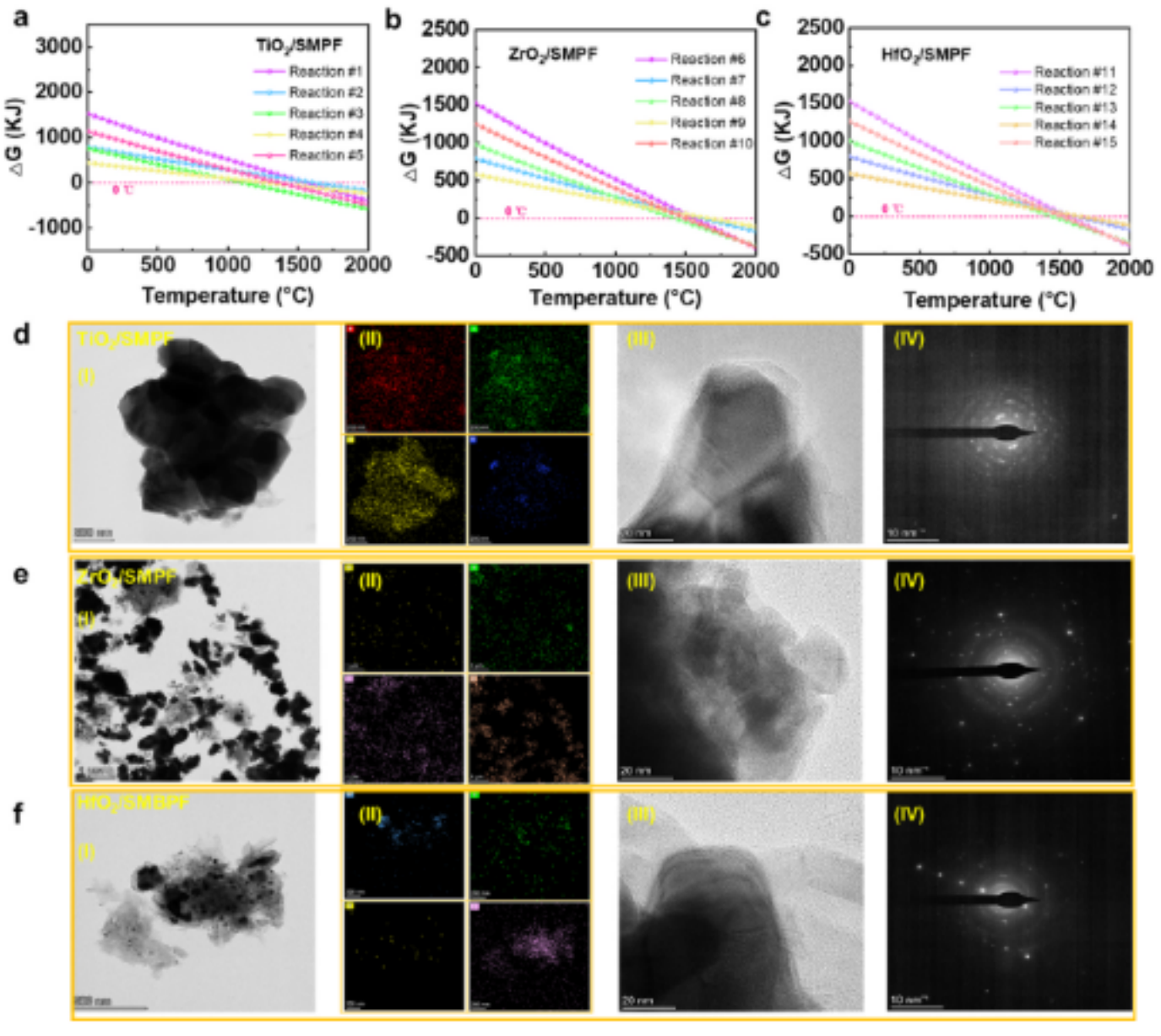

Fig. 7. Analysis of the ceramization mechanism of SMCPCs. a-c) The ΔG-temperature curves of potential reactions during the sintering process of SMCPCs. d) The TEM images of TiO_2/SMPF sintered product. e) The TEM images of ZrO_2/SMPF sintered product. f) The TEM images of HfO_2/SMPF sintered product. (All tested samples contained 20 wt% ceramic fillers.)

A comparable ceramization pathway is observed in the HfO_2/SMPF system. Thermodynamic calculations predict favorable formation of HfC at elevated temperatures (Fig. 7c), which is supported by TEM observations (Fig. 7f). Hf-based ceramic particles are embedded within and encapsulated by a continuous graphitized carbon layer, elemental mapping and high-resolution imaging confirm the coexistence of HfC, residual HfO_2, and carbon phases. The above results indicate that, SMCPC mainly undergoes thermal decomposition and carbon thermal reduction reactions during the ceramization process, and the incorporated B_2O_3 participates in the high-temperature evolution process through its liquid-phase fluxing effect, which promotes the bonding of ceramic-carbon phases and contributes to the formation of a denser and more continuous ceramic structure. This process results in a multiphase ceramic structure, whose composition includes metallic carbides, residual metal oxides, and graphitized carbon. These phases are interconnected to form a relatively dense and continuous ceramic-carbon framework during high-temperature ceramization. The multiphase ceramic structure suppresses oxygen diffusion and reduces the direct erosion of the internal matrix by high-temperature airflow, thereby inhibiting thermochemical ablation and structural denudation under extreme thermal environments.

3.6. Potential applications of SMCPCs in high-temperature deformation structures

SMCPC demonstrates significant potential for application in high-temperature deformation structures. The self-adaptive TPS concept proposed in this work is based on a sequential thermally triggered transition process involving shape recovery, carbonization, and subsequent ceramization, as illustrated in Fig. 8a. For SMCPCs, the shape recovery process can be activated once the material temperature exceeds the shape transition temperature. Through compositional design, the recovery temperature of SMCPCs can be adjusted within the range of 94–144 °C, enabling controllable deployment behavior under different thermal environments. The TGA and DTG results reveal that significant decomposition of the phenolic backbone begins above approximately 400 °C. Therefore, the shape recovery process can be completed before severe thermal degradation occurs, ensuring that the material can fully recover to the designed initial shape during deployment. After the onset of thermal decomposition, the polymer matrix gradually loses its shape memory capability, which is beneficial for maintaining the recovered geometry. As the external temperature further increases, SMCPCs progressively undergo carbonization (above 800 °C) and subsequent ceramization reactions, whose characteristic temperatures depend on the specific ceramic filler system. During this process, the high-char-yield phenolic matrix and the gradually formed multiphase ceramic framework continuously enhance the stability of the recovered

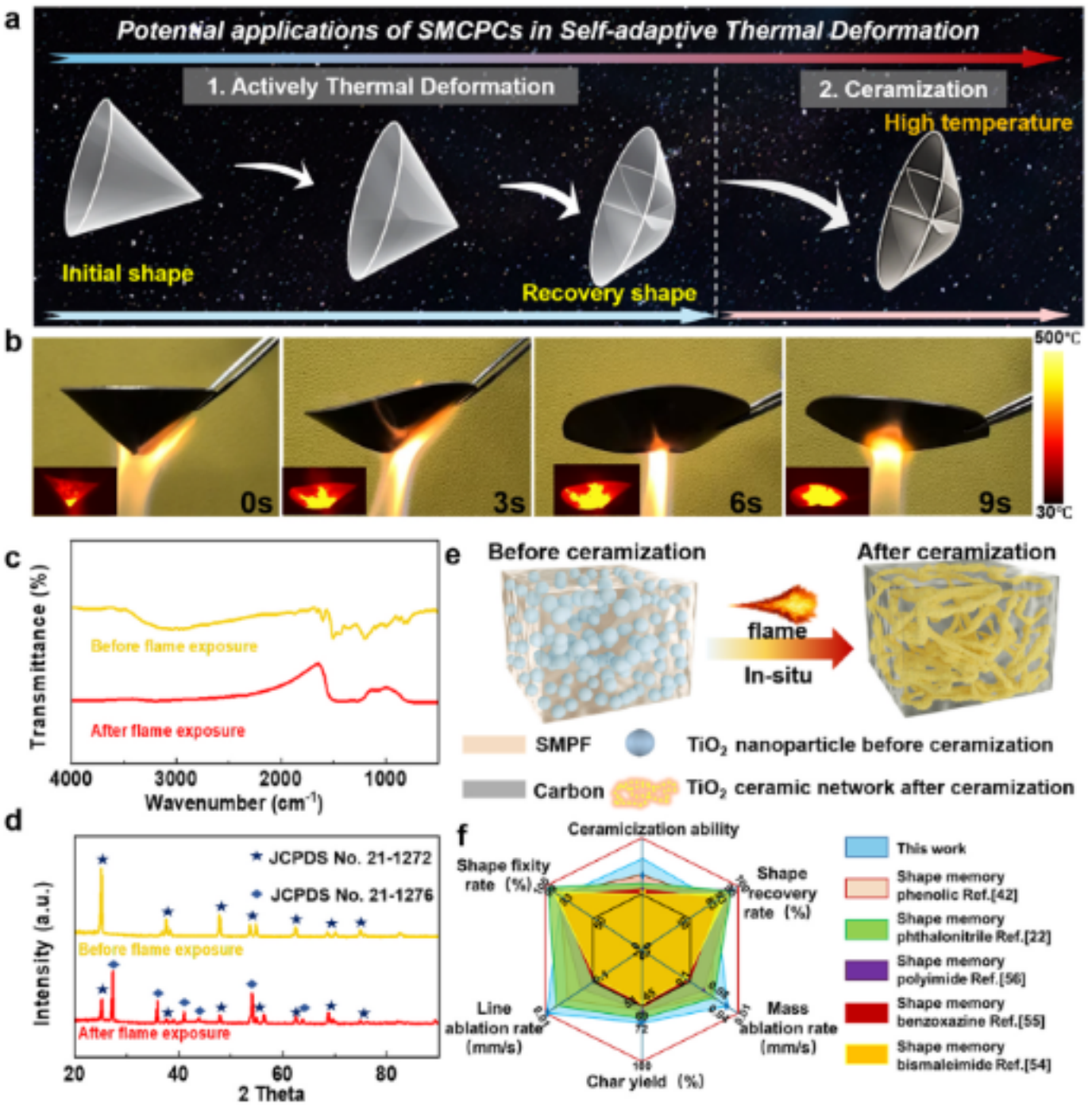

Fig. 8. Demonstration of SMCPCs for potential application. a) Schematic illustration of the "deformation–recovery–ceramization" behaviors of SMCPC. b) Images showing the shape recovery process of the 20 wt% TiO_2/SMPF model under flame heating. (Inset: infrared thermal imaging images.) c) The infrared spectra of 20 wt % TiO_2/SMPF before and after flame exposure. d) The XRD curves of 20 wt% TiO_2/SMPF before and after flame exposure. e) Schematic illustration of the ceramization process of SMCPC. f) Radar chart comparing the performance of SMCPC with current high-temperature resistant shape memory materials. (The scales for shape recovery rate, shape fixity rate, and char yield range from 0 to 100, while the scales for mass ablation rate and line ablation rate are arranged logarithmically from 10^{0} to 10^{-2}.)

structure. Consequently, the recovered structure can be gradually transformed into a ceramic architecture capable of maintaining shape stability under high-temperature conditions, thereby enabling the complete self-adaptive TPS process.

As a conceptual verification of high-temperature deformation performance, we fabricated TiO_2/SMPF into a conical configuration. When the sample was exposed to a flame environment, the bottom of the cone, which first contacted the flame, initiated shape recovery, followed by the remaining regions. Under flame heating, the surface temperature of the material reached 447 °C (as shown in the inset of Fig. 8b), and the structure completely recovered into an umbrella-like configuration after 9 s. With continued flame exposure, the material underwent ceramization, which stabilized the recovered shape as a permanent structure. The change in chemical composition of TiO_2/SMPF after exposure to a flame environment is the direct reason for its ability to maintain a permanent shape. The chemical structural evolution was investigated by infrared spectroscopy (Fig. 8c). After being burned by the flames, the characteristic absorption bands of the phenolic resin matrix disappear entirely, which indicates complete pyrolysis and carbonization of SMPF. Combined with the XRD analysis results (Fig. 8d), it can be observed that a phase transition of TiO_2 from anatase (PDF#21-1272) to the thermodynamically more stable and mechanically harder rutile phase (PDF#21-1276), together with the emergence of additional diffraction features.

The microstructure of TiO_2/SMPF changed significantly after the high-temperature experiment, as shown in Fig. S13. Prior to the experiment, TiO_2 particles were uniformly dispersed in the polymer matrix with a near-spherical morphology. After the experiment, the material transformed into a porous ceramic architecture composed of interlocking rod-like TiO_2 units. High-magnification observations reveal a pronounced morphology transition from spherical particles to elongated crystalline rods under high-temperature. The growth and interconnection of these rods form a continuous three-dimensional network that provides stable geometric support to the ceramicized structure, as illustrated in Fig. 8e. These results demonstrate that ceramization simultaneously drives the conversion of the organic matrix into a carbon phase and promotes crystal rearrangement and phase evolution of TiO_2, leading to the formation of a robust ceramic framework.

As shown in Fig. 8f, in comparison to the previously reported high-temperature resistant shape memory materials, such as shape memory bismaleimide [54], shape memory phthalonitrile [22], shape memory phenolic [42], shape memory benzoxazine [55] and shape memory polyimide [56], the SMCPCs developed in this study demonstrate remarkable integrated performance, including excellent shape memory performance (shape fixity rate of 99.0%, shape recovery rate of 93%), high char yield (more than 71% at 1000 °C), good ablation resistance (line ablation rate of 0.008 mm/s, mass ablation rate of 0.038 g/s) and ceramization ability.

Overall, the results demonstrate that the synergistic integration of shape memory behavior and high-temperature ceramization enables SMCPCs to achieve efficient shape recovery, enhanced mechanical performance, and ablation resistance under extreme thermal environments. The introduction of ceramic fillers not only improves the thermal stability and load-bearing capability of the composites, but also promotes the formation of a dense multiphase ceramic framework during high-temperature exposure, thereby ensuring structural stability. These combined advantages position SMCPC as a promising new generation of intelligent high-temperature deformation materials for aerospace applications.

4. Conclusion

In summary, this work introduces a synergistic design strategy that integrates shape memory functionality with high-temperature ceramization, resulting in SMCPCs with enhanced shape memory, thermal resistance, and structural toughening capabilities. The phenolic–boric acid copolymer network ensures stable shape memory behavior (shape transition temperature of 94–144 °C), while incorporating metal oxides and boron oxide facilitates in situ ceramic transformation at high temperatures. By optimizing the ceramic filler content, the composites achieved significantly improved mechanical properties and thermal stability (char yield of 71.7% at 1000 °C), while maintaining excellent shape memory performance (shape fixity rate of 99% and shape recovery rate of 93%). Meanwhile, a thermal conduction model was established to predict and analyze the temperature distribution during ablation as well as the improvement in ablation resistance induced by different fillers, which establishes a solid structural basis for applications in high-temperature environments and ceramization. Through XPS, XRD and microstructure analysis, we clarified the ceramization mechanism of SMCPCs. The multi-phase ceramic framework composed of metal carbides, metal oxides and graphitized carbon jointly enhanced its thermal stability, ablation resistance and load-bearing capacity in high-temperature environments. As a proof of concept, we preliminarily validate the feasibility of SMCPCs for high-temperature thermoresponsive adaptive shape adjustment. The SMCPCs enriches the options for high-temperature resistant smatrt materials and demonstrates significant potential for aerospace applications. Although the present SMCPCs demonstrate excellent integrated performance, several challenges still remain for practical applications. The intrinsic brittleness of phenolic-based composites still needs to be further optimized to improve their toughness and impact resistance under complex service environments. In addition, the long-term durability and cyclic stability of SMCPCs under repeated thermal-mechanical coupling conditions require further investigation. Future work will focus on optimizing interfacial compatibility and lightweight design, enhancing the toughness of phenolic composites, as well as developing multifunctional smart materials with improved environmental adaptability and engineering applicability.

CRediT authorship contribution statement

Likai Hu: Conceptualization, Data curation, Investigation, Methodology, Writing – original draft. **Fenghua Zhang:** Funding acquisition, Resources, Supervision, Writing – review & editing. **Binghuan Gao:** Formal analysis, Methodology, Validation. **Lan Luo:** Formal analysis, Writing – review & editing. **Yanju Liu:** Formal analysis, Funding acquisition, Validation, Writing – review & editing. **Jinsong Leng:** Conceptualization, Resources, Supervision, Writing – review & editing.

Declaration of competing interest

The authors declare that they have no known competing financial interests or personal relationships that could have appeared to influence the work reported in this paper.

Acknowledgements

We thank the National Natural Science Foundation of China (Grant No. 92271206 and No. 92271112) and Science and Technology Department of Heilongjiang Province (2024ZXDXA23) for the support of this work.

Appendix. ASupplementary data

Supplementary data to this article can be found online at https://doi.org/10.1016/j.compositesb.2026.113908.

Data availability

Data will be made available on request.

References

[1] Li G, Feng Y, Fuh J, Liu Q, Zhao J, Wu W, et al. 4D printing of highly maneuverable robots: controllable power amplification behaviours of stimulus-response materials. Adv Mater 2026;38:e16070. https://doi.org/10.1002/adma.202516070.

[2] Wang L, Wang F, Jin F, Wang X, Sang L, Zhao Y. 4D printing of continuous fiber-reinforced hybrid lattice structures with electrothermally controlled shape memory behavior. Compos Part B Eng 2026;313:113410. https://doi.org/10.1016/j.compositesb.2026.113410.

[3] Rahmatabadi D, Khajepour M, Bayati A, Mirasadi K, Yousefi M, Shegeft A, et al. Advancing sustainable shape memory polymers through 4D printing of polylactic acid-polybutylene adipate terephthalate blends. Eur Polym J 2024;216:113289. https://doi.org/10.1016/j.eurpolymj.2024.113289.

[4] Rahmatabadi D, Youseft M, Shamsolhodaei S, Baniassadi M, Abrinia K, Baghani M, et al. 4D printing of polyethylene glycol-grafted carbon nanotube-reinforced polyvinyl chloride-polycaprolactone composites for enhanced shape recovery and thermomechanical performance. Adv Intell Syst 2025;7:2500113. https://doi.org/10.1002/aisy.202500113.

[5] Wang Z, Si M, Han J, Wu Y, Zhang T, Chen T. Photoinduced, swift, and reversible spatiotemporal programming of double dynamically bonded liquid crystal elastomer actuators. Adv Mater 2025;37:2501815. https://doi.org/10.1002/adma.202501815.

[6] Wan X, Chen S, Ma J, Dong C, Banerjee H, Laperrousaz S, et al. Multimaterial shape memory polymer fibers for advanced drug release applications. Adv Fiber Mater 2025;7:1576–89. https://doi.org/10.1007/s42765-025-00571-4.

[7] Cui H, Miao S, Esworthy T, Lee S, Zhou X, Hann S, et al. A novel near-infrared light responsive 4D printed nanoarchitecture with dynamically and remotely controllable transformation. Nano Res 2019;12:1381–8. https://doi.org/10.1007/s12274-019-2340-9.

[8] Yu Y, Zhang F, Liu Y, Leng J. Smart polymer fibers: promising advances in microstructures, stimuli-responsive properties and applications. Adv Fiber Mater 2025;7:1010–41. https://doi.org/10.1007/s42765-025-00539-4.

[9] Youseft M, Rahmatabadi D, Majid B, Baniassadi M, Bodaghi M. 4D printing of multifunctional and biodegradable PLA-PBAT-Fe_3O_4 nanocomposites with supreme Mechanical and shape memory properties. Macromol Rapid Commun 2024;46:2400661. https://doi.org/10.1002/marc.202400661.

[10] Wang Q, Sun H, Zou C, Chen C. Photo-, thermal-, and electro-responsive polyolefin-based actuators. Angew Chem Int Ed 2026;65:e23449. https://doi.org/10.1002/anie.202523449.

[11] Zeng C, Liu L, Bian W, Liu Y, Leng J. 4D printed electro-induced continuous carbon fiber reinforced shape memory polymer composites with excellent bending resistance. Compos Part B Eng 2020;194:108034. https://doi.org/10.1016/j.compositesb.2020.108034.

[12] Sun X, Zhang Q, Chi D, Wu C, Wang X, Xu L, et al. Programmable shape recovery onset temperatures via phase-separated dual-network polymers. Adv Funct Mater 2026:e26834. https://doi.org/10.1002/adfm.202526834. 0.

[13] Ni C, Zhang C, Qin Z, Ke Q, Wu B, Zhou X, et al. 4D printing of trigger-free shape-memory hydrogels towards self-adaptive substrates for bioelectronics. Nat Commun 2025;17:677. https://doi.org/10.1038/s41467-025-67323-1.

[14] Zhang X, Guo S, Wei G, Zhang H, Hao X, Tan S, et al. 4D printing shape memory PLA/Co/CNTOH composites with adaptive microwave absorption for reconfigurable metastructures. Compos Part B Eng 2025;306:112798. https://doi.org/10.1016/j.compositesb.2025.112798.

[15] Hu L, Zhang F, Luo L, Leng J. Advances in shape memory polymer porous materials: fabrications, microstructures, and applications. Research 2025;8:989. https://doi.org/10.34133/research.0989.

[16] Youseft M, Rahmatabadi D, Ahmadi M, Bayati A, Baniassadi M, Laachachi A, et al. 4D printing for minimally invasive biomedical applications: programmable smart materials for deployable devices, drug delivery, and tissue regeneration. Mater Des 2026;263:11555. https://doi.org/10.1016/j.matdes.2026.115555.

[17] Mirasadi K, Youseft M, Jin L, Rahmatabadi D, Baniassadi M, Liao W, et al. 4D printing of magnetically responsive shape memory polymers: toward sustainable solutions in soft robotics, wearables, and biomedical devices. Adv Sci 2025;13:e13091. https://doi.org/10.1002/advs.202513091.

[18] Ni C, Chen D, Yin Y, Wen X, Chen X, Yang C, et al. Shape memory polymer with programmable recovery onset. Nature 2023;622:748–53. https://doi.org/10.1038/s41586-023-06520-8.

[19] Du B, Zhang X, Wang T, He Y, Shen M, Yu T. Three-Dimensional printable color-modulation and shape-programmable structures: an encryption key for image recognition electronic locks. Research 2025;8:666. https://doi.org/10.34133/research.0666.

[20] Bai Y, Zhu S, Liang J, Xing R, Kong J. 4D printing of magnetically responsive materials and their applications. Research 2025;8:847. https://doi.org/10.34133/research.0847.

[21] Hu R, Zhang F, Luo L, et al. An end-capping strategy for shape memory phthalonitrile resins via annealing enables conductivity and wave-absorption. Chem Eng J 2024;489:150956. https://doi.org/10.1016/j.cej.2024.150956.

[22] Hu R, Zhang F, Luo L, Wang L, Liu Y, Leng J. Reconfigurable high-temperature thermal protection shape memory aerogel based on phthalonitrile resin with facile template method. Carbon 2025;242:120378. https://doi.org/10.1016/j.carbon.2025.120378.

[23] Yue J, Qin M, Yu H, He Q, Feng W. Superelastic graphene-based composite aerogel for thermal and electromagnetic protection in extreme temperature environments. Adv Funct Mater 2025;39:2508319. https://doi.org/10.1002/adfm.202508319.

[24] Liu H, Yang Z, Qi H, Wang T, Wang Q. Engineering intermolecular dynamic hydrogen bond interaction to regulate the tribology behaviors of shape memory polyimide. Chem Eng J 2025;523:168441. https://doi.org/10.1016/j.cej.2025.168441.

[25] Zhao W, Zhang A, Li X, Bian J, Yang S, Ni K, et al. Novel flexible polyether segment polybenzoxazine shape memory nanocomposites reinforced by incorporating functionalized carbon nanotubes. Compos Part B Eng 2025;292:112104. https://doi.org/10.1016/j.compositesb.2024.112104.

[26] Yang S, He Y, Leng J. Shape memory poly (ether ether ketone)s with tunable chain stiffness, mechanical strength and high transition temperatures. Int J Smart Nano Mater 2022;13:1–16. https://doi.org/10.1080/19475411.2022.2053228.

[27] Jiang X, Chu F, Zhou X, Li X, Jia P, Luo X, et al. Construction of bismaleimide resin with enhanced flame retardancy and mechanical properties based on a novel DOPO-Derived bismaleimide monomer. J Colloid Interface Sci 2022;614:629–41. https://doi.org/10.1016/j.jcis.2022.01.152.

[28] Liu G, Zhang X, Lu X, Zhao Y, Zhou Z, Xu J, et al. 4D additive-subtractive manufacturing of shape memory ceramics. Adv Mater 2023;35:e2302108. https://doi.org/10.1002/adma.202302108.

[29] Kong D, Guo A, Wu H, Li X, Wu J, Hu Y, et al. Four-dimensional printing of polymer-derived ceramics with high-resolution, reconfigurability, and shape memory effects. Addit Manuf 2024;83:104050. https://doi.org/10.1016/j.addma.2024.104050.

[30] Wu J, Guo A, Wu H, Ma J, Qu P, Wang S, et al. Programmable polylactic acid-ceramics 4D printing with shape memory function. Virtual Phys Prototyp 2025;20:2505621. https://doi.org/10.1080/17452759.2025.2505621.

[31] Wang R, Yuan C, Cheng J, He X, Ye B, Jian B, et al. Direct 4D printing of ceramics driven by hydrogel dehydration. Nat Commun 2024;15:758. https://doi.org/10.1038/s41467-024-45039-y.

[32] Liu G, Zhao Y, Wu G, Lu J. Origami and 4D printing of elastomer-derived ceramic structures. Sci Adv 2018;4:eaat0641. https://doi.org/10.1126/sciadv.aat06.

[33] Mao Z, Yu H, Yu Z, Tang Z, Li K, Osman A, et al. Biomimetic TPMS structure-based entangled hydrogel for efficient solar-driven atmospheric water harvesting. Adv Mater 2025;0:e15166. https://doi.org/10.1002/adma.202515166.

[34] Chen S, Li J, Shi H, Chen X, Liu G, Meng S, et al. Lightweight and geometrically complex ceramics derived from 4D printed shape memory precursor with reconfigurability and programmability for sensing and actuation applications. Chem Eng J 2023;455:140655. https://doi.org/10.1016/j.cej.2022.140655.

[35] Liu T, Xue T, Yang S, Zhang X, Zhang C, Fan W, et al. Ultralight and ablation-resistant shape-memory ceramizable polymer aerogel for self-adaptive thermal protection. Adv Mater 2026;38:e15166. https://doi.org/10.1002/adma.202516627.

[36] Chen X, Shi K, Gu Z, Quan H, Huang D, Zhang Y, et al. Positive effects of anisotropic thermal conductive structure of phenolic based composites on enhancing thermal protection. Compos Part B Eng 2025;292:112093. https://doi.org/10.1016/j.compositesb.2024.112093.

[37] Wang Y, Wang Q, Lv S, Zou B, Chen L, Cao T, et al. Investigation on thermal conductivities of plain-woven carbon/phenolic and silica/phenolic composites at high temperature: theoretical prediction and experiment. Compos Sci Technol 2024;256:110771. https://doi.org/10.1016/j.compscitech.2024.110771.

[38] Liu Y, Deng Z, Zhang W, Jiang G, Cao Z, Huang Z, et al. Lightweight, high-strength, heat-resistant TiB_2-B_4C-modified phenolic aerogel/carbon fiber composites with excellent thermal stability, oxidation, and ablation resistance for thermal protection. Adv Compos Hybrid Mater 2025;8:110771. https://doi.org/10.1007/s42114-024-01106-y.

[39] Xu B, Wang F, Yang X, Huang Z. Bioinspired fabrication of lightweight gradient ceramizable phenolic aerogel composites with exceptional ablation resistance and thermal insulation for superior thermal protection system. Corros Sci 2026;258:113382. https://doi.org/10.1016/j.corsci.2025.113382.

[40] Deng Y, Zhang F, Liu Y, Leng J. Design and synthesis of shape memory phenol-formaldehyde with good irradiation resistance, thermal, and mechanical properties. ACS Appl Polym Mater 2022;4:5789–99. https://doi.org/10.1021/acsapm.2c00719.

[41] Hu L, Luo L, Zhang F, Liu Y, Leng J. Design and preparation of shape memory phenol-formaldehyde foam composites with excellent thermal stability and mechanical properties. Compos Part A Appl Sci Manuf 2023;174:107738. https://doi.org/10.1016/j.compositesa.2023.107738.

[42] Hu L, Luo L, Zhang F, Liu Y, Leng J. Self-sensing shape memory boron phenolic-formaldehyde aerogels with tunable heat insulation for smart thermal protection systems. Chem Eng J 2025;505:159558. https://doi.org/10.1016/j.cej.2025.159558.

[43] Zhao J, Chen F, Shen Y, Liu S, Liu S. A glass-ceramic approach to prepare porous TiO_2 with self-supported nano-flakes: the phase evolution and the thermal stability of the product. Ceram Int 2022;48:18745–52. https://doi.org/10.1016/j.ceramint.2022.03.149.

[44] Li T, Liu Z, Jia Y, Shen Q, Tang L, Yao X, et al. ZrO_2 short-fiber-reinforced oxide scale enabling superior cyclic ablation resistance in C/C-ZrC-SiC composites prepared by reaction melt infiltration. Compos Part B Eng 2026;313:113380. https://doi.org/10.1016/j.compositesb.2025.113380.

[45] Shen Z, Liu Z, Mu R, He L, Liu G. Y–Er–ZrO_2 thermal barrier coatings by EB-PVD: thermal conductivity, thermal shock life and failure mechanism. Appl Surf Sci Adv 2021;3:100043. https://doi.org/10.1016/j.apsadv.2020.100043.

[46] Bahamirian M, Keyvani A, Irankhah R, Farvizi M. High-temperature cyclic oxidation of micro- and nano-ZrO_2–25wt.%CeO_2–2.5wt.%Y_2O_3 thermal barrier coatings at 1300 °C. Surf Coat Technol 2023;474:130076. https://doi.org/10.1016/j.surfcoat.2023.130076.

[47] Chu Y, Sun W, Tian T, Xiong X, Zhang H. Effect of sintering additives on the sintering and ablation resistance of novel HfO_2-ThO_2 high-temperature multiphase oxides. Ceram Int 2023;49:18977–87. https://doi.org/10.1016/j.ceramint.2023.03.023.
[48] Sun J, Li T, Reitz A, Fu Q, Riedel R, Yu Z. High-temperature stability and oxidation behavior of SiOC/HfO2 ceramic nanocomposite in air. Corros Sci 2020;175:108866. https://doi.org/10.1016/j.corsci.2020.108866.
[49] Yan X, Ma B, Hong C, Jin X, Zhang J, Wu C, et al. Volume radiation-ablation thermal response model and analysis of lightweight needled quartz fiber/phenolic aerogel composite. Int J Therm Sci 2026;220:110377. https://doi.org/10.1016/j.ijthermalsci.2025.110377.
[50] Alan C, Stephen J. The role of thermal and transport properties on the binder burnout of injection-molded ceramic components. Chem Eng J 1998;71:243–52. https://doi.org/10.1016/S1385-8947(98)00098-9.
[51] Huang Z, Jiang G, Yang X, Wang Y, Deng Z. Ablation behavior and mechanism of Ti_3SiC_2 modified carbon fiber/boron phenolic resin ceramizable composite. Polym Degrad Stab 2024;230:111035. https://doi.org/10.1016/j.polymdegradstab.2024.111035.
[52] Jiang Z, Li J, Sun G, Luo W, Zhao P. Effect of B_2O_3 additive on the microstructure and luminescent properties of spark plasma sintered YAG: ce transparent ceramics. J Alloy Compd 2024;1008:176637. https://doi.org/10.1016/j.jallcom.2024.176637.
[53] Xiong Y, Chen J, Song K, Xie T, Xia G, Ma X, et al. Sintering activation energy and low-temperature sinterable process of Boron-lanthanide glass/$Li_2Zn_3Ti_4O_{12}$ ceramic composite systems for LTCC technology. Ceram Int 2024;50(24):52797–807. https://doi.org/10.1016/j.ceramint.2024.10.133.
[54] Li Y, Zhang F, Liu Y, Leng J. A tailorable series of elastomeric-To-rigid, selfhealable, shape memory bismaleimide. Small 2023;20:202307244. https://doi.org/10.1002/smll.202307244.
[55] Luo L, Niu Z, Hu R, Zhang F, Liu Y, Leng J. Triple-shape memory polybenzoxazine resins and their composites. Compos Part A Appl Sci Manuf 2024;177:107910. https://doi.org/10.1016/j.compositesa.2023.107910.
[56] Wang X, Xin X, Xing Y, Zhang D, Kong D, Leng J. Multimonomer regulation-based high strength, high modulus, high toughness shape memory polyimide and kresling origami structures. Chem Eng J 2025;526:170950. https://doi.org/10.1016/j.cej.2025.170950.